

Dynamic Tumor-Specific MHC-II Immuno-PET Predicts Checkpoint Inhibitor Immunotherapy Efficacy in Melanoma

Running title: MHC-II PET Imaging for Immunotherapy

Zhen Yang^{1,2#}, Feng Li^{1,2#}, Yuqian Huang^{2,3}, Na Yin⁴, Junjun Chu⁵, Ying Ma⁶, Roderic I. Pettigrew⁷, Dale J. Hamilton^{2,8}, Diego R. Martin^{1,9}, and Zheng Li^{1,2,9*}

#joint first authors

¹Department of Radiology, ²Center for Bioenergetics, Houston Methodist Academic Institute, Texas, USA; ³Xiangya Hospital, Central South University, Hunan, China; ⁴Department of Pediatrics, Baylor College of Medicine, Texas, USA; ⁵Department of Medicine, Kech School of Medicine, USC, California, USA; ⁶NIBIB, NIH, Maryland, USA; ⁷Engineering Medicine, Texas A&M University, Texas, USA; ⁸Department of Medicine, ⁹Department of Radiology, Weil Cornell Medicine, New York, USA

* Corresponding author:

Zheng Li, 6670 Bertner Ave, Houston, TX 77030; 713-441-7962; zli@houstonmethodist.org

First author:

Zhen Yang, 6670 Bertner Ave, Houston, TX 77030; 713-363-8494; zyang@houstonmethodist.org

Feng Li, 6670 Bertner Ave, Houston, TX 77030; 713-441-3501; fli2@houstonmethodist.org

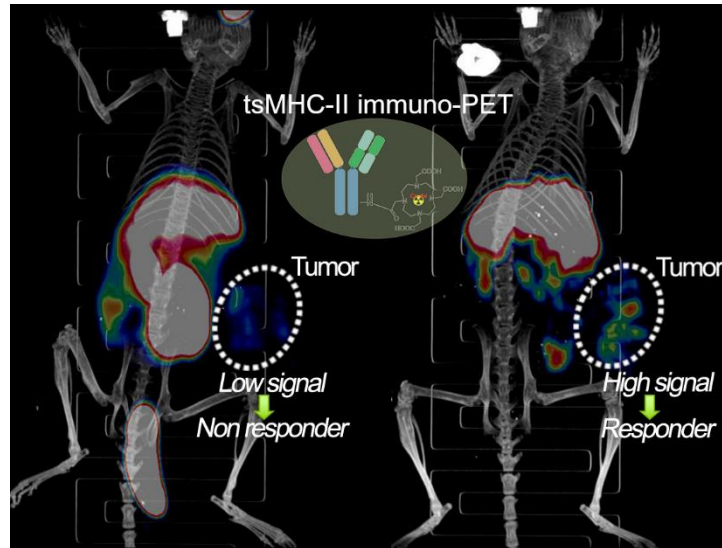
ABSTRACT

Despite the advance of immunotherapy, only a small subset of patients gains long-term survival benefit. It warrants a compelling rationale to develop immuno-PET imaging that could predict tumor response to the immunotherapy. An increasing number of studies have shown that tumor-specific major histocompatibility complex II (tsMHC-II) associates with improved responses to targeted immunotherapy. The aim of this study was to investigate the potential of tsMHC-II protein expression and its dynamic change upon treatment with interferon γ (IFN γ) as a new target for immuno-PET to predict response to immunotherapy. **Methods:** Major histocompatibility complex II (MHC-II) antibody was radiolabeled with DOTA-chelated ^{64}Cu to derive an MHC-II immuno-PET tracer. Two melanoma models (B16SIY, B16F10), which are responder and non-responder to PD1/PD-L1 checkpoint inhibitor, respectively, were used. Both tumor models were treated with anti-PD1 and IFN γ , which enabled observation of dynamic change of tsMHC-II. Small-animal PET imaging, biodistribution and histological studies were performed to validate the correlation of tsMHC-II with the tumor response to the immunotherapy. **Results:** FACS analysis of the two tumors supported the consensual recognition of tsMHC-II correlated to the tumor response to the immunotherapy. The *in vivo* PET imaging revealed higher basal levels of tsMHC-II in the responder, B16SIY, than in the non-responder, B16F10. When treated with anti-PD1 antibody in animals, B16SIY tumors displayed a sensitive increase of tsMHC-II compared to B16F10 tumors. In IFN γ stimulation groups, the greater magnitude of tsMHC-II was further amplified when the IFN γ signaling is activated in the B16SIY tumors, which positively upregulates tsMHC-II in the tumor immunity. Subsequent histopathological analysis supported the correlative characteristics of tsMHC-II with tumor immunity and response to cancer immunotherapy. **Conclusion:** Collectively, the predictive value of tsMHC-II immuno-PET was validated for stratifying tumor immunotherapy responders vs. non-responders. Monitoring sensitivity of tsMHC-II to IFN γ stimulation may provide an effective strategy to predict the tumor response to immunotherapy.

Keywords: immuno-PET, MHC-II, anti-PD1 immunotherapy, melanoma, molecular imaging

GRAPHIC ABSTRACT

We describe herein a tumor-specific MHC-II (tsMHC-II) immuno-PET imaging to provide predictive value of tumor response to immunotherapy. This tool may guide oncologists in the selection of patients for immunotherapy.



INTRODUCTION

The discovery of immune checkpoint molecules utilized by cancer cells to evade the patient's immune system, have spurred development of immune checkpoint inhibitors (ICI) to disrupt inhibitory ligand-receptor interactions (1). The primary ICI molecules, cytotoxic T-lymphocyte antigen 4, programmed cell death 1 (PD1), and programmed cell death ligand 1 (PD-L1), facilitate a blockade strategy that unleashes antitumor T-cells to recognize and eradicate tumor cells across multiple types of cancer. ICI-modulated immunotherapy, which is now FDA-approved for the treatment of a broad range of tumor types, has revolutionized the cancer treatment landscape. Unfortunately, only a small subset of patients gains long-term survival benefit from the ICI therapy, while a sizable number of patients do not experience a durable clinical response (2,3). The variable success of ICI-modulated therapy provides a compelling rationale for the development of predictive tools to identify ICI-responder vs. ICI-non-responder patients to optimize resource utilization, improve clinical outcomes, and avoid unnecessary toxicity.

A predictive biomarker for ICI therapy is PD-L1 expression; current clinical practice relies on excisional biopsies to sample patient tumors and test for PD-L1 (4). Since the assay requires invasive sampling of tumor tissue and is compromised by sampling errors and tumor heterogeneity, it is not ideal. In addition, immune checkpoint molecule expression is dynamic and can be upregulated by host immune response and inflammatory cytokines. Given the recently emerged reports that patients without PD-L1 expression also respond to PD1/PD-L1 axis targeted ICI therapy (5), new biomarkers that accurately predict ICI therapy outcome are needed.

PET imaging, which permits noninvasive whole-body visualization of tumor and immune cell characteristics, provides unique insights into the mechanisms of action, and failure, of ICI immunotherapy (6). For instance, ¹⁸F-fluorodeoxyglucose (¹⁸F-FDG) PET/CT scan can potentially predict patient response to ICI therapy (7-9). Routinely used in oncology for staging and monitoring cancer patients, ¹⁸F-FDG PET has proven useful. However, a major challenge in delineating immunotherapy response with ¹⁸F-FDG PET is that the uptake of ¹⁸F-FDG can be complicated by glucose metabolism modulators, which is not specific to immunotherapy. Another approach is to use immuno-PET that combines PET radioisotopes with targeting antibodies (Abs) to image immune checkpoint biomarkers. This approach enables noninvasive assessment of immune checkpoint biomarker expression levels in both primary tumors and metastatic lesions

(6,10). The expression of immune checkpoint molecules may correlate with therapeutic response, thereby improving patient selection for ICI therapy. The availability of ICI molecules, including targeting antibodies, engineered fragments, or binders for PD1/PD-L1 immune checkpoint axis, have fueled development of ICI-targeted PET tracers (4,11-13). As an additional advantage, imaging tumor-associated immune components with the immuno-PET may offer useful information about the patient's tumor microenvironment (14,15).

Tumor-specific major histocompatibility complex II (tsMHC-II) expression has been reported to associate with prognosis of PD1/PD-L1 immunotherapy and major histocompatibility complex II (MHC-II) molecules are required for tumor antigen presentation. The downregulation of MHC-II in numerous malignancies implicates the immune system control of cancer progression and evolution (16,17). The expression of tsMHC-II is a critical biomarker for tumor antigen presentation in melanoma and may predict anti-PD1/PD-L1 therapy response (18). The promising role of MHC-II neoantigens in tumor immunity provided a compelling rationale for us to develop an MHC-II immuno-PET tracer that detects tsMHC-II and to investigate its predictive value for tumor response to immunotherapy. PET imaging was attempted to image MHC-II expressed on myeloid cells which associated with tumor microenvironment for immune response prediction (19). We geared the effort to develop PET imaging for noninvasively assessment of tsMHC-II expression and validate its predicative value to immune responses (14,20,21).

MATERIALS AND METHODS

DOTA Conjugation and Radiolabeling

MHC-II Ab (0.2 ml; 7 mg/mL) was added to 200 μ L DOTA-NHS-Ester phosphate-buffered saline solution (PBS) solution (0.15 mg, 0.75 mg/ml). NaOH (10 μ L; 0.1M) was added to adjust to pH 8~9. The reaction mixture was stirred in the dark at 0 $^{\circ}$ C for six hours. The crude product was purified by PD-10 chromatography. The DOTA-MHCII fraction was collected and used for radiolabeling. Conjugation of DOTA on MHC- ab was confirmed by mass spectrometry.

For radiolabeling, ^{64}Cu -Acetate (^{64}Cu -Cu(OAc)₂), $^{64}\text{CuCl}_2$ (185 MBq in 0.1 M HCl) was combined with 300 μ L 0.1 M ammonium acetate (pH 5.6), vortexed, and incubated for 15 min at room temperature. DOTA-MHCII (50 μ L) in PBS (200 μ L) was mixed with ^{64}Cu - Acetate (37-74 MBq), and incubated at 30 $^{\circ}$ C for 60 min. ^{64}Cu -DOTA-MHCII was purified by PD-10

chromatography; radiochemical yield = 55~70%. Calculated specific activity was 92.5-118.4 MBq/mg.

Murine B16 Melanoma Models

Murine B16F10 melanoma cells (American Type Culture Collection) and B16SIY cells engineered from B16F10 to express SIYRYYYGL (SIY) antigen were treated similarly, *i.e.*, Dulbecco's Modified Eagle Medium supplemented with 10% fetal bovine serum. Cells were cultured in 5% CO₂ at 37 °C and used at 75% confluence.

All animal studies were approved by the Institutional Animal Care and Use Committee of the Houston Methodist Research Institute. To generate the murine melanoma models, 1×10^6 cells were harvested and suspended into 100 μ L Matrigel diluted with 1:1 PBS, and subcutaneously injected into the left flank of mice. Each melanoma model, B16F10 and B16SIY, was challenged with vehicle (Ctrl group), anti-PD1 (anti-PD1 group), and IFN γ (IFN γ group). Briefly, the anti-PD1 challenged group received three consecutive intraperitoneal injections of anti-mouse PD1 antibody (120 μ g per mouse) every other day after which the tumor was ~ 100 - 200 mm^3 . Post-anti-PD1 treatment mice (bearing tumors $\sim 600 \text{ mm}^3$) were used for PET imaging and the subsequent biodistribution study. For IFN γ stimulation, mice with tumors at $\sim 600 \text{ mm}^3$ were each given a single intraperitoneal injection of 10 μ g recombinant mouse IFN γ at 24 h before PET imaging. Basal level tsMHC-II expression in mice was based on PET images when tumors reached $\sim 600 \text{ mm}^3$.

Small-animal PET/CT Imaging and Biodistribution Study

Small-animal PET/CT scans were performed and analyzed using Siemens Inveon PET/CT imaging system. Approximately 3.7 MBq ⁶⁴Cu-DOTA-MHCII (33 μ g Ab) was intravenously injected into tumor-bearing mice (n = 6) via the tail vein. In-line PET and CT scans were acquired at 24 h and 48 h post injection (p.i.) and images were obtained using manufacture's 2-dimensional ordered-subsets expectation maximum algorithm. Two control PET imaging studies were performed to validate the specificity of the radiotracer with the following blocking agents: (a) non-radiolabeled MHC-II antibody; and (b) non-radiolabeled rat IgG2b isotype control. Detailed blocking study and PET/CT image processing were described in [Supplemental Materials](#). After the 48 h p.i. imaging scans, mice were sacrificed to evaluate radiotracer biodistribution between

major organs. The radioactivity accumulated in each tissue was measured using 2470 Wizard2 Automatic Gamma Counter (Perkin Elmer) and calculated as radioactivity divided by tissue weight and decay-corrected injected dose to express as %ID/g.

Histopathological, Western Blotting and Flow Cytometry Assays

Tumor tissues were collected after terminal PET/CT scans and fixed in 4% paraformaldehyde for overnight, followed by processing, paraffin embedding, and sectioning into 4-5 μm tissue sections. The sections were deparaffinized in xylene, a series of ethanol solutions, then treated with 0.3% hydrogen peroxide for 20 min, followed by incubation in 5% horse serum block for 10 min prior to addition of MHC-II primary antibody. Detection was performed with HRP-conjugated respective secondary system followed by diaminobenzidine and counter staining with hematoxylin solution. For immunofluorescence staining, the sections were immunofluorescence stained with Texas Red anti-rat IgG. Images were captured using an inverted fluorescence microscope.

Tumor tissues from a separate cohort (n = 6) were collected for western blotting of tsMHC-II expression. Briefly, fresh tumor samples were collected, homogenized, and lysed in 0.1 Triton X-100 buffer. The lysed samples were electrophoresed in SDS-PAGE gels (Bio-Rad) following protein quantification by BCA Protein Assay according to manufacturer's protocol with equivalent protein amounts loaded for each group. Proteins were blotted onto PVDF membranes by wet transfer. The membranes were probed with MHC-II antibody and secondary antibody and were developed using enhanced chemiluminescence reagent; images were acquired using the ChemiDoc gel documentation system.

Another cohort (n = 6) was used to analyze tumors by flow cytometry. The tumor tissues were freshly harvested and ground into small bits in 2% FBS supplemented RPMI1640 medium. The cell suspension was filtered through a 40 μm cell strainer, washed with 1% BSA supplemented PBS, and centrifuged at 500 x g for 5 min. The cell pellet was collected and re-suspended for subsequent antibody staining. 100 μl /tube of 10^6 cells suspended in 1% BSA PBS were incubated with fluorescent mAbs specific to anti-mouse MHC-II (FITC anti-mouse MHC-II, BioLegend, #107606), PD-L1 (PE anti-mouse PD-L1, BioLegend, #124308), and CD-45 (APC anti-mouse CD45, BioLegend, #103112) at RT for 30 minutes. Tubes were washed twice with 1 mL 1% BSA

PBS and centrifuged at 500 x g for 5 minutes. The stained cell data were acquired and analyzed using BD LSRFortessa Flow Cytometer.

Statistics

Quantitative data was expressed as mean \pm SD. Means were compared using the Student *t* test. 95% confidence level was chosen to determine the significance between groups, and *P* value of less than 0.05 was considered statistically significant.

RESULTS

We first sought to validate the correlation of tsMHC-II with its immune response in melanomas. FACS analysis revealed the basal level and dynamic change of tsMHC-II expression in two distinct murine melanomas, B16F10 and B16SIY, low and good responder, respectively (14,20,21). The leucocyte-associated biomarker, CD45, was used to segregate tumor cells (CD45⁻) from other immune cells (CD45⁺). CD45⁻/MHC-II⁺ population was considered as tsMHC-II population. The FACS result showed a mildly higher (**P*=0.0382) basal level of tsMHC-II in immune-responder B16SIY (46.8% \pm 5.1%) compared with immune-non-responder B16F10 (33.3% \pm 3.6%) (Fig. 1). Importantly, the tsMHC-II in B16SIY increased (81.6% \pm 9.8%) following stimulation by the immunity activator, IFN γ , which also increased tsMHC-II in B16F10 (51.0% \pm 5.8%); however, the magnitude of increase was less profound than that in B16SIY. In contrast, treatment of tumors with anti-PD1 antibody increased tsMHC-II over basal levels in B16F10 (48.1% \pm 5.4%) and B16SIY (60.9% \pm 6.8%). Meanwhile, tsMHC-II expression levels in anti-PD1-treated remained higher in B16SIY than that in B16F10. Of note, the increase of tsMHC-II was more profound following IFN γ stimulation vs. anti-PD1 treatment in the immunity-responding B16SIY tumor, whereas the difference between IFN γ stimulation and anti-PD1 treatment in the immunity-non-responding B16F10 tumor was absent. These data confirmed the positive correlation of tsMHC-II with tumor-immune response. More importantly, compared to immunity non-responder, upregulation of tsMHC-II in immunity-responder tumors was more sensitive to immunity perturbation, particularly, IFN γ stimulation.

In addition, PD-L1 expression in tumor was analyzed in the same cohort. Both basal expression and change of PD-L1 were similar between B16F10 and B16SIY in several ways: 1) baseline expression of PD-L1 in B16F10 was 24.3% \pm 4.2% and in B16SIY, it was 29.4% \pm 5.6%;

2) the PD-L1 expression was similarly increased to $38.8\% \pm 5.6\%$ and $40.8\% \pm 6.2\%$ for B16F10 and B16SIY tumors, respectively; 3) notably, when stimulated with IFN γ , increased PD-L1 expression in B16F10 and B16SIY correlated similarly with tsMHC-II expression, $69.7\% \pm 9.8\%$ and $74.7\% \pm 10.1\%$, respectively. However, there was no distinctive change between B16F10 tumors and B16SIY tumors, in PD-L1 expression in either baseline ($P=0.34$) or anti-PD1/IFN γ -stimulated groups. Comparison of tsMHC and PD-L1 in B16F10 and B16SIY (Fig. 1B) reveal that tsMHC-II manifests as a sensitive correlation with tumor response to the immunotherapy, whereas a similar correlation was not found in the assessment of PD-L1 expression in tumor. Therefore, we reasoned that tsMHC-II and its preferential induction by IFN γ immune perturbation have better predictive value for therapeutic inhibition of the PD1/PD-L1 axis.

To noninvasively image the tsMHC-II, murine MHC-II Ab was chemically modified with DOTA chelator. After conjugation, the reaction was quenched and analyzed using mass spectrometry to confirm chelator conjugated on MHC-II Ab following literature procedure (22). Immunofluorescence staining and western blot assays revealed no significant change in the immunoreactivity of the antibody toward the MHC-II target upon chemical conjugation (Fig. Supplemental Figure 1-3). Afterwards, the DOTA conjugated MHC-II Ab was radiolabeled with ^{64}Cu isotope to obtain a MHC-II immuno-PET tracer (^{64}Cu -DOTA-MHCII) for noninvasive *in vivo* imaging of tsMHC-II in murine B16F10 and B16SIY tumor models. Higher baseline ^{64}Cu -DOTA-MHCII uptake was observed in B16SIY vs. B16F10 tumors (Fig. 2). After IFN γ stimulation, ^{64}Cu -DOTA-MHCII uptake increased more in immune-responder B16SIY vs. non-responder B16F10 tumors, whereas anti-PD1 treatment increased tumor uptake, with a magnitude that was less prominent than that of IFN γ .

ROI analysis of tumor uptake (Fig. 3A) confirmed the distinctive tsMHC-II expression pattern in the two tumor models: 1) ^{64}Cu -DOTA-MHCII uptake was 2.75 fold higher (** $P=0.0082$) in B16SIY (1.1 ± 0.2 %ID/g) than in B16F10 tumors (0.4 ± 0.1 %ID/g) in control groups; 2) likewise, B16SIY exhibited higher uptake of ^{64}Cu -DOTA-MHCII in tumor (1.8 ± 0.3 %ID/g) than that of B16F10 (0.7 ± 0.2 %ID/g) when treated with anti-PD1 antibody (** $P=0.0035$); 3) IFN γ stimulation further amplified ^{64}Cu -DOTA-MHCII uptake in B16SIY tumor (3.2 ± 0.4 %ID/g), which is 2.9 fold higher than that of B16F10 (1.1 ± 0.2 %ID/g) (** $P=0.0002$). By comparing the tumor uptake of ^{64}Cu -DOTA-MHCII tracer in control groups with IFN γ stimulated groups, the

dynamic change of tsMHC-II expression was derived. We saw that the change of tsMHC-II induced by IFN γ in B16SIY (### $P=0.0003$) was greater than that in B16F10 (# $P=0.034$). Similar change by anti-PD1 treatment in real time was also analyzed. However, no significant change was observed in B16F10 ($P=0.0862$) and a less potent difference was observed in B16SIY ($P=0.0092$).

Biodistribution analysis further confirmed distinctive tumor uptake of the ^{64}Cu -DOTA-MHCII tracer in B16F10 and B16SIY at baseline as well as under the anti-PD1 and IFN γ treated conditions (Fig. 3B). IFN γ stimulation and anti-PD1 treatment upregulated systemic MHC-II in both tumor models (Fig. 3C and 3D). The distinctive imaging pattern of tumor uptake of the ^{64}Cu -DOTA-MHCII tracer in B16F10 and B16SIY confirmed that noninvasive imaging of tsMHC-II at baseline and IFN γ -induced dynamic change may be used to distinguish immune-responder vs. non-responder tumors.

Specificity of the tracer was thoroughly tested using additional controls (Supplemental Figure 4-6). Blocking study using excessive non-radiolabeled MHC-II Ab showed obvious reduction of tumor-uptake signal, which supported the specific binding of ^{64}Cu -DOTA-MHCII tracer in the PET imaging. In addition, blocking study with excessive non-radiolabeled IgG was performed, and showed no dramatic effect of the tumor uptake. It ruled out significant non-specific uptake of the radiotracer resulting from Fc receptor. When we closely examined biodistribution change of the radiotracer in the blocking studies, excessive blocking with non-radiolabeled MHC-II Ab seemed diminished the accumulation of radiotracer in liver and spleen. But the changes were not deemed significant within the current dataset. As for the blocking using IgG isotype, no significant change was observed in biodistribution of the radiotracer.

Western blot assay showed a higher tsMHC-II expression at baseline in B16SIY vs. B16F10 tumors in the control samples (Fig. 4A-B). Anti-PD1 treated and IFN γ stimulated B16SIY vs. B16F10 tumors expressed more tsMHC-II. Notably, the tsMHC-II expression was increased when induced by anti-PD1 treatment and IFN γ stimulation and the dynamic change was prominently higher in B16SIY tumor than in the B16F10 tumor. Similar tsMHC-II expression pattern was also observed in the immunohistochemistry assay (Fig. 4C).

We further performed immunofluorescence staining to examine the origin of the MHC-II positive cells. The majority of MHC-II positive cells are CD45 negative (Fig. 5A), supporting the conclusion that different MHC-II expression patterns were due to tumor cells. When the quantified

MHC-II fluorescence was normalized by the CD45 negative cell numbers, a positive correlation of tsMHC-II with the response of tumor to immunotherapy was derived, which was consistent with the results obtained in the *in vivo* PET imaging as well as the FACS analyses (Fig. 5B). By noninvasive imaging, the histopathological study supported that: 1) immune-responsive tumors exhibit a high level of tsMHC-II expression even at baseline; 2) expression is sensitive to immune perturbation and could be preferentially elevated by IFN γ stimulation; 3) tsMHC-II immuno-PET noninvasively assessed the basal tsMHC-II as well as its dynamic change upon immunity stimulation, which provided promising predictive value for identifying tumor responding to immunotherapy from the non-responders.

DISCUSSION

Recent clinical studies have revealed that the specific haplotype of MHC-II, HLA-DR, expressed on tumors represented tumor-autonomous phenotype and associated with its response to the targeted immunotherapy (18, 23, 24). Currently, no *in vivo* PET imaging targeting the HLA-DR has been reported to further validate the idea. Herein, we selected two murine melanoma tumors with distinctive responses to immunotherapy to investigate the predictive value of tsMHC-II immuno-PET imaging (14,20,21). Commercially available anti-mouse MHC-II antibody was used to target the tsMHC-II, and its specificity was validated in the binding assays prior to the *in vivo* PET imaging. Worthy noting is that specific HLA-DR immuno-PET tracer can be developed to further translation to human studies.

Our FACS analysis showed a consistent result with the report that tsMHC-II positively correlates with tumor response to cancer immunotherapy (18,23). Furthermore, the *in vivo* tsMHC-II immuno-PET imaging clearly distinguished B16SIY and B16F10 tumors by noninvasively assessing tsMHC-II. This observation was further corroborated by *ex vivo* histopathological studies and biochemical assay of the tumor tissue collected from the same cohort used in the *in vivo* studies. Collectively, these data support the hypothesis that tsMHC-II expression is associated with tumor response to immunotherapy, and that noninvasive imaging of tsMHC-II using the immuno-PET delineates the characteristic tsMHC-II expression.

Cells and molecules that regulate the immune system are dynamically changed upon immune stimulation. PD-L1 is involved in the anti-PD1/PD-L1 axis blockade immunotherapy and thereby rationalized as a biomarker to distinguish responding tumors from non-responders

(4,13,24,25). However, some tumors were identified with negligible PD-L1 expression at basal level but preferentially induced dynamic increase of PD-L1 expression in tumor by immune response, and thereby, may still benefit from the immunotherapy. Therefore, the sensitivity of tsMHC-II to dynamic change in tumor immunity, specifically, raised by therapeutic anti-PD1 blockade that targets PD1/PD-L1 immunotherapy axis, was also examined in this study. Whereas the B16SIY tumor still had a higher level of MHC-II positivity and ⁶⁴Cu-DOTA-MHCII PET signal than that of B16F10 tumor, the dynamic changes stimulated by anti-PD1 treatment were not as significant when compared to the basal levels. Tumor immunity and inflammation often involve IFN γ signaling, and IFN γ preferentially induces upregulation of MHC-II expression on tumor cells to promote tumor immunity (26-29). PET imaging is a useful tool for monitoring response to tumor immunotherapy (11). So, we additionally examined the dynamic change of tsMHC-II upon IFN γ stimulation. This comparison determined that a greater magnitude of IFN γ -induced increase of MHC-II expression on tumor cells occurred in the B16SIY tumor with the better immunity response than that in B16F10 tumor with a lower immunity response. These findings suggest that tsMHC-II immuno-PET imaging could be used to monitor tsMHC-II at basal level and IFN γ -stimulated dynamic change, raising the possibility that the combined high manifestations could be used as a reliable prospective indicator of good response to cancer immunotherapy.

CONCLUSION

In conclusion, we uncovered a correlation between tsMHC-II and tumor immunity with response to checkpoint inhibitor immunotherapy in murine melanoma by PET. The newly developed ⁶⁴Cu-DOTA-MHCII PET tracer captured the characteristic tsMHC-II in melanoma and provided noninvasive imaging of dynamic tsMHC-II expression. The distinctive tsMHC-II immuno-PET images from immune-responder and immune-non-responder tumors revealed that tsMHC-II is a promising predictive biomarker for tumor response to cancer immunotherapy. Monitoring tsMHC-II at baseline and IFN γ -stimulated dynamic change could be used to effectively identify immune-responder patients from non-responders before immunotherapy to avoid unnecessary side effects.

DISCLOSURE

This work was funded by Houston Methodist Academic Institute and foundation. No other potential conflict of interest relevant to this article exist.

ACKNOWLEDGMENTS

This work was supported by the Houston Methodist Academic Institute (HMAI) and foundation. We thank Dr. Henry Pownall and Kimberly Greer for revision of the paper and we also thank the preclinical imaging core facility of HMAI. This research was funded in part through NIH U54CA210181, R01CA245920-02, Finger Distinguished Endowed Chair and MD Anderson Distinguished Endowed Chair.

KEY POINTS

QUESTION: A new immuno-PET tracer was developed to predict tumor response to immunotherapy

PERTINENT FINDINGS: TsMHC-II and its dynamic modulation was validated to correlate with tumor response to immunotherapy. MHC-II antibody derived immuno-PET imaging showed in vivo assessment of tsMHC-II and thereby provided predictive value of tumor response to the immunotherapy.

IMPLICATIONS FOR PATIENT CARE: Monitoring tsMHC-II at baseline and IFN γ -stimulated dynamic change could be used to effectively identify immune-responder patients from non-responders before immunotherapy to avoid unnecessary side effects.

REFERENCES

1. Wei SC, Duffy CR, Allison JP. Fundamental mechanisms of immune checkpoint blockade therapy. *Cancer Discov.* 2018;8:1069-1086.
2. Fares CM, Van Allen EM, Drake CG, Allison JP, Hu-Lieskovan S. Mechanisms of resistance to immune checkpoint blockade: why does checkpoint inhibitor immunotherapy not work for all patients? *Am Soc Clin Oncol Educ Book.* 2019;39:147-164.
3. Barrieto L, Caminero F, Cash L, Makris C, Lamichhane P, Deshmukh RR. Resistance to checkpoint inhibition in cancer immunotherapy. *Transl Oncol.* 2020;13:100738-100748.
4. Patel SP, Kurzrock R. PD-L1 Expression as a predictive biomarker in cancer immunotherapy. *Mol Cancer Ther.* 2015;14:847-856.
5. Havel JJ, Chowell D, Chan TA. The evolving landscape of biomarkers for checkpoint inhibitor immunotherapy. *Nature Rev Cancer.* 2019;19:133-150.
6. Mayer AT, Gambhir SS. The immunoimaging toolbox. *J Nucl Med.* 2018;59:1174-1182.
7. Cho SY, Lipson EJ, Im H-J, et al. Prediction of response to immune checkpoint inhibitor therapy using early-time-point 18F-FDG PET/CT imaging in patients with advanced melanoma. *J Nucl Med.* 2017;58:1421-1428.
8. Tao X, Li N, Wu N, et al. The efficiency of 18F-FDG PET-CT for predicting the major pathologic response to the neoadjuvant PD-1 blockade in resectable non-small cell lung cancer. *Eur J Nucl Med Mol Imaging.* 2020;47:1209-1219.
9. Seban R-D, Mezquita L, Berenbaum A, et al. Baseline metabolic tumor burden on FDG PET/CT scans predicts outcome in advanced NSCLC patients treated with immune checkpoint inhibitors. *Eur J Nucl Med Mol Imaging.* 2020;47:1147-1157.
10. van de Donk PP, Kist de Ruijter L, Lub-de Hooge MN, et al. Molecular imaging biomarkers for immune checkpoint inhibitor therapy. *Theranostics.* 2020;10:1708-1718.
11. Gibson HM, McKnight BN, Malysa A, et al. IFN γ PET imaging as a predictive tool for monitoring response to tumor immunotherapy. *Cancer Res.* 2018;78:5706-5717.
12. Auslander N, Zhang G, Lee JS, et al. Robust prediction of response to immune checkpoint blockade therapy in metastatic melanoma. *Nature Med.* 2018;24:1545-1549.
13. Broos K, Lecocq Q, Raes G, Devoogdt N, Keyaerts M, Breckpot K. Noninvasive imaging of the PD-1:PD-L1 immune checkpoint: embracing nuclear medicine for the benefit of personalized immunotherapy. *Theranostics.* 2018;8:3559-3570.
14. Zhang Y, Fang C, Wang RE, et al. A tumor-targeted immune checkpoint blocker. *Proc Natl Acad Sci.* 2019;116:15889-15894.
15. Depontieu FR, Qian J, Zarling AL, et al. Identification of tumor-associated, MHC class II-restricted phosphopeptides as targets for immunotherapy. *Proc Natl Acad Sci.* 2009;106:12073-12078.

16. Thibodeau J, Bourgeois-Daigneault M-C, Lapointe R. Targeting the MHC class II antigen presentation pathway in cancer immunotherapy. *Oncoimmunology*. 2012;1:908-916.
17. Topalian SL. MHC class II restricted tumor antigens and the role of CD4+ T cells in cancer immunotherapy. *Curr Opin Immunol*. 1994;6:741-745.
18. Johnson DB, Estrada MV, Salgado R, et al. Melanoma-specific MHC-II expression represents a tumour-autonomous phenotype and predicts response to anti-PD-1/PD-L1 therapy. *Nature Commun*. 2016;7:10582-10592.
19. Rashidian M, Keliher EJ, Bilate AM, et al. Noninvasive imaging of immune responses. *Proc Natl Acad Sci*. 2015;112:6146-6151.
20. Meng Y, Efimova EV, Hamzeh KW, et al. Radiation-inducible immunotherapy for cancer: senescent tumor cells as a cancer vaccine. *Mol Ther*. 2012;20:1046-1055.
21. Spranger S, Koblish HK, Horton B, Scherle PA, Newton R, Gajewski TF. Mechanism of tumor rejection with doublets of CTLA-4, PD-1/PD-L1, or IDO blockade involves restored IL-2 production and proliferation of CD8(+) T cells directly within the tumor microenvironment. *J Immunother Cancer*. 2014;2:3-17.
22. Alam IS, Mayer AT, Sagiv-Barfi I, et al. Imaging activated T cells predicts response to cancer vaccines. *J Clin Investig*. 2018;128:2569-2580.
23. Alspach E, Lussier DM, Miceli AP, et al. MHC-II neoantigens shape tumour immunity and response to immunotherapy. *Nature*. 2019;574:696-701.
24. Axelrod ML, Cook RS, Johnson DB, Balko JM. Biological consequences of MHC-II expression by tumor cells in cancer. *Clin Cancer Res*. 2019;25:2392-2402.
25. Lv G, Qiu L, Sun Y, et al. PET imaging of tumor PD-L1 expression with a highly specific non-blocking nanobody. *J Nucl Med*. 2019;61:117-122.
26. Teng F, Meng X, Kong L, Yu J. Progress and challenges of predictive biomarkers of anti PD-1/PD-L1 immunotherapy: a systematic review. *Cancer Lett*. 2018;414:166-173.
27. Bhat MY, Solanki HS, Advani J, et al. Comprehensive network map of interferon gamma signaling. *J cell commun signal*. 2018;12:745-751.
28. Steimle V, Siegrist CA, Mottet A, Lisowska-Grospierre B, Mach B. Regulation of MHC class II expression by interferon-gamma mediated by the transactivator gene CIITA. *Science*. 1994;265:106-109.
29. Giroux M, Schmidt M, Descoteaux A. IFN- γ -induced MHC Class II expression: transactivation of class II transactivator promoter IV by IFN regulatory factor-1 is regulated by protein kinase C- α . *J Immunol*. 2003;171:4187-4194.

Figure Legends

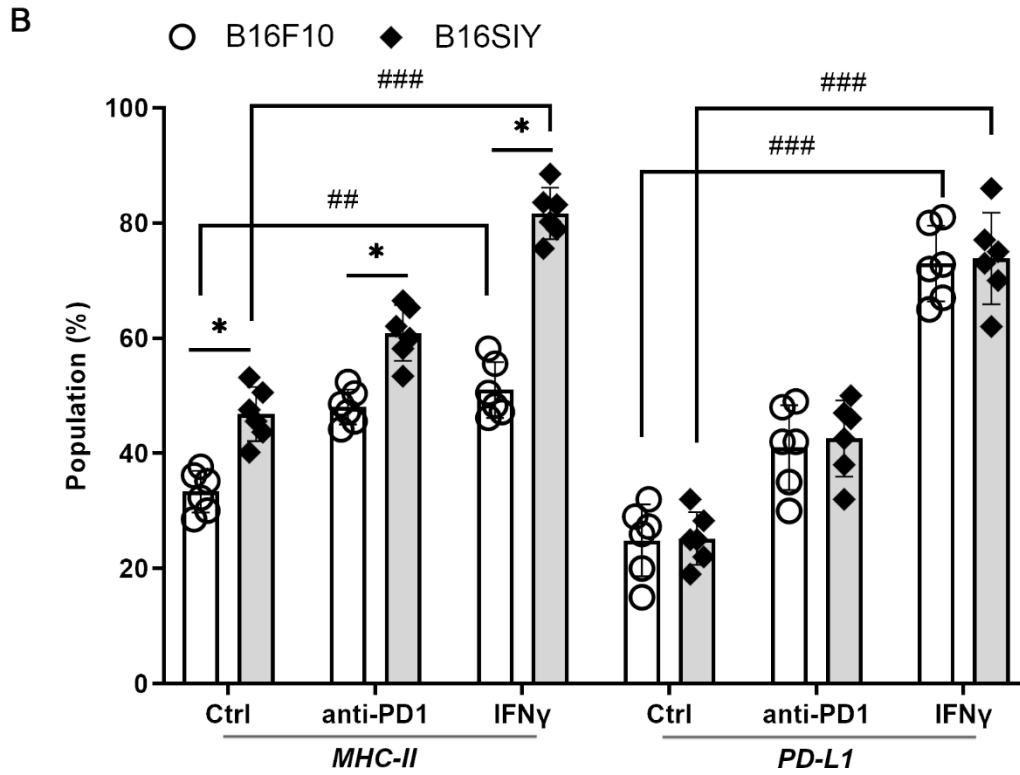
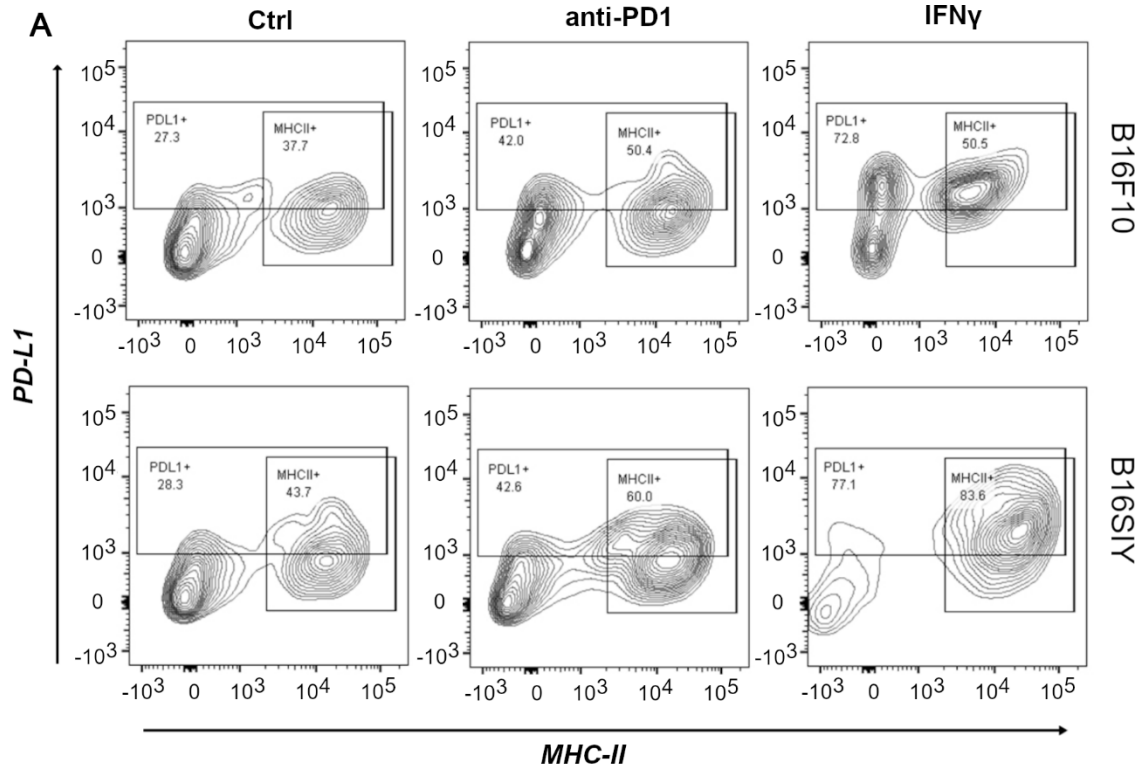


FIGURE 1. (A) FACS analysis of tsMHC-II and PD-L1 population in B16F10 and B16SIY tumors and the population changes when treated with anti-PD1 and IFN γ immunity stimulants. (B) Summary of the FACS assay (n=6 for each cohort). Statistical analysis for MHC-II: B16F10.Ctrl vs. B16SIY.Ctrl (*, $P=0.0382$); B16F10.PD1 vs. B16SIY.PD1 (*, $P=0.0158$); B16F10.IFN γ vs. B16SIY.IFN γ (*, $P=0.0112$); B16F10.Ctrl vs. B16F10.IFN γ ($\#$, $P=0.0026$); B16SIY.Ctrl vs. B16SIY.IFN γ ($\#\#\#$, $P=0.0001$). Statistical analysis for PD-L1: B16F10.Ctrl vs. B16F10.IFN γ ($\#\#\#$, $P=0.0001$); B16SIY.Ctrl vs. B16SIY.IFN γ ($\#\#\#$, $P=0.0001$).

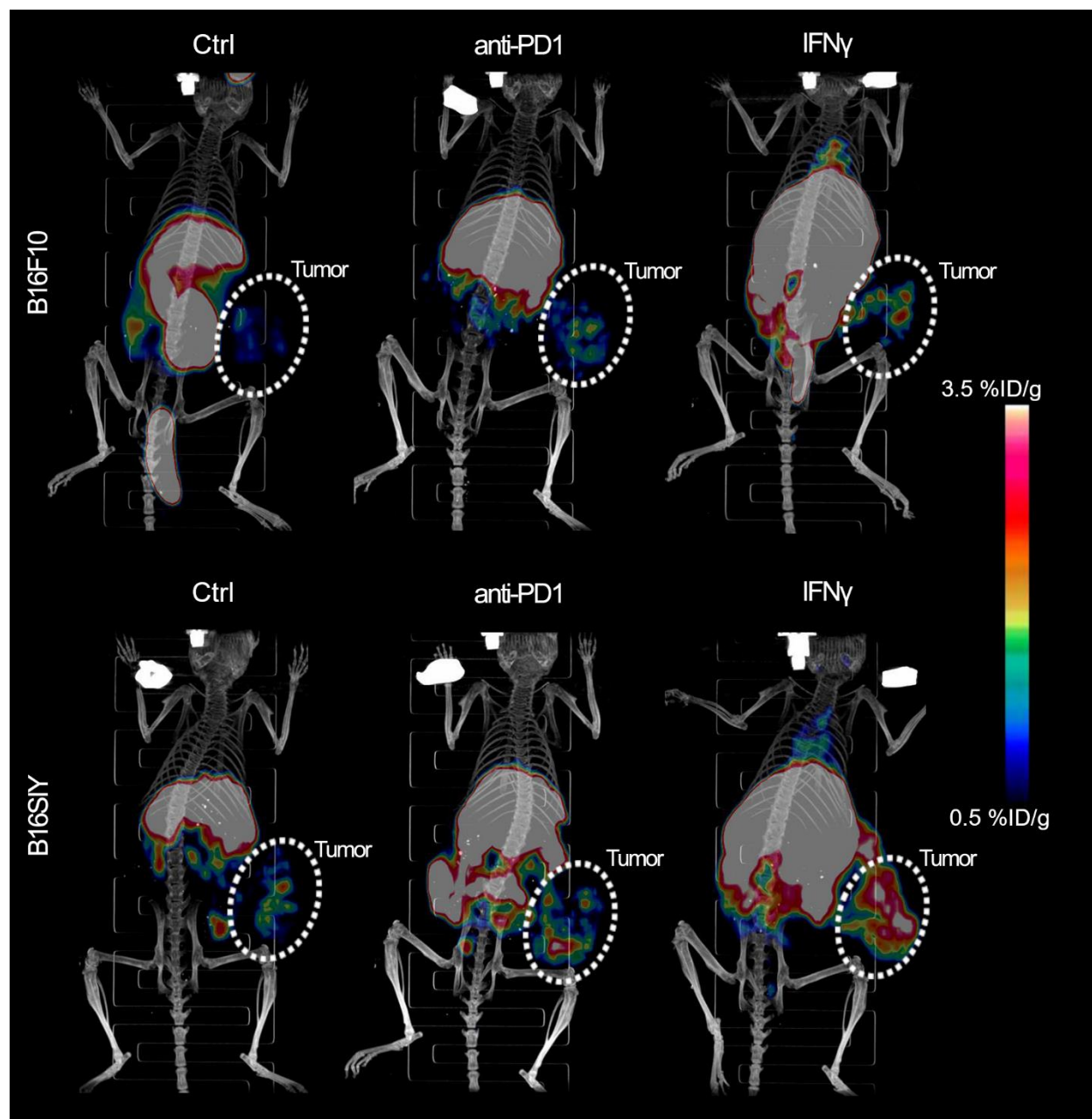


FIGURE 2. 3D-rendered maximum intensity projection (MIP) of the PET-CT images of control, anti-PD1 treated, and IFN γ stimulated B16F10 and B16SIY tumor-bearing mice after 48-hour injection of ^{64}Cu -DOTA-MHCII. The circle areas indicate the tumor site.

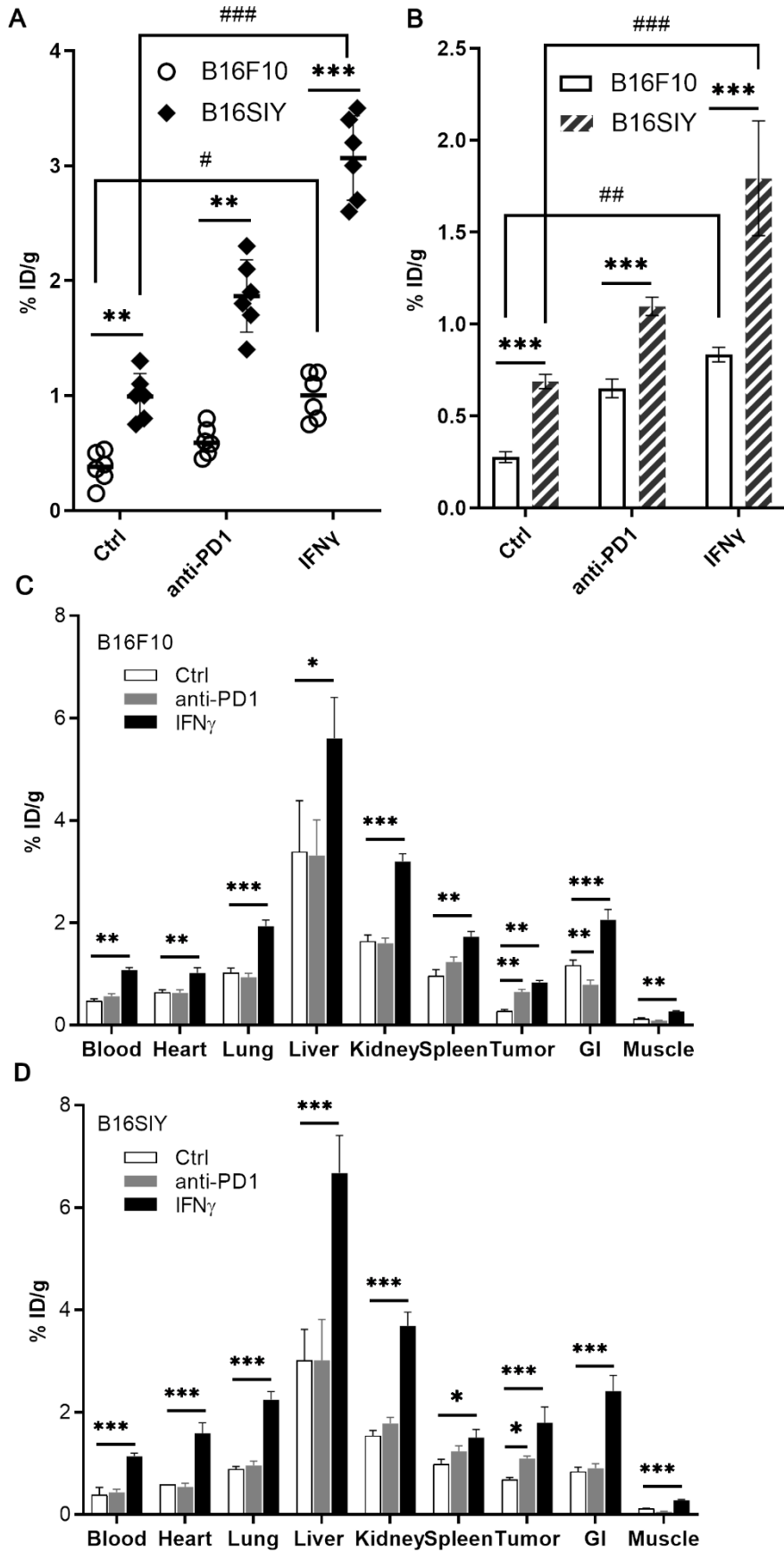


FIGURE 3. (A) ROI quantification of tumor accumulated ^{64}Cu -DOTA-MHCII in PET images (n=6 per group). An unpaired student t test was performed to compare: B16F10.Ctrl vs. B16SIY.Ctrl (**, $P=0.0082$); B16F10.PD1 vs. B16SIY.PD1 (**, $P=0.0035$); B16F10.IFN γ vs. B16SIY.IFN γ (***, $P=0.0002$); B16F10.Ctrl vs. B16F10.IFN γ (#, $P=0.034$); B16SIY.Ctrl vs. B16SIY.IFN γ (###, $P=0.0003$); (B) Tumor uptake of ^{64}Cu -DOTA-MHCII in 48 hours post injection biodistribution study. An unpaired student t test was performed to compare: B16F10.Ctrl vs. B16SIY.Ctrl (***, $P=0.0002$); B16F10.PD1 vs. B16SIY.PD1 (***, $P=0.0003$); B16F10.IFN γ vs. B16SIY.IFN γ (***, $P=0.0002$); B16F10.Ctrl vs. B16F10.IFN γ (##, $P=0.0044$); B16SIY.Ctrl vs. B16SIY.IFN γ (###, $P=0.0001$); (C) Biodistribution study of ^{64}Cu -DOTA-MHCII in B16F10 tumor model. (D) Biodistribution study of ^{64}Cu -DOTA-MHCII in B16SIY tumor model. (n=6 for biodistribution study, * $P < 0.05$, ** $P < 0.01$ and *** $P < 0.001$ show statistical difference as compared with Ctrl group). Gastrointestinal is abbreviated as GI.

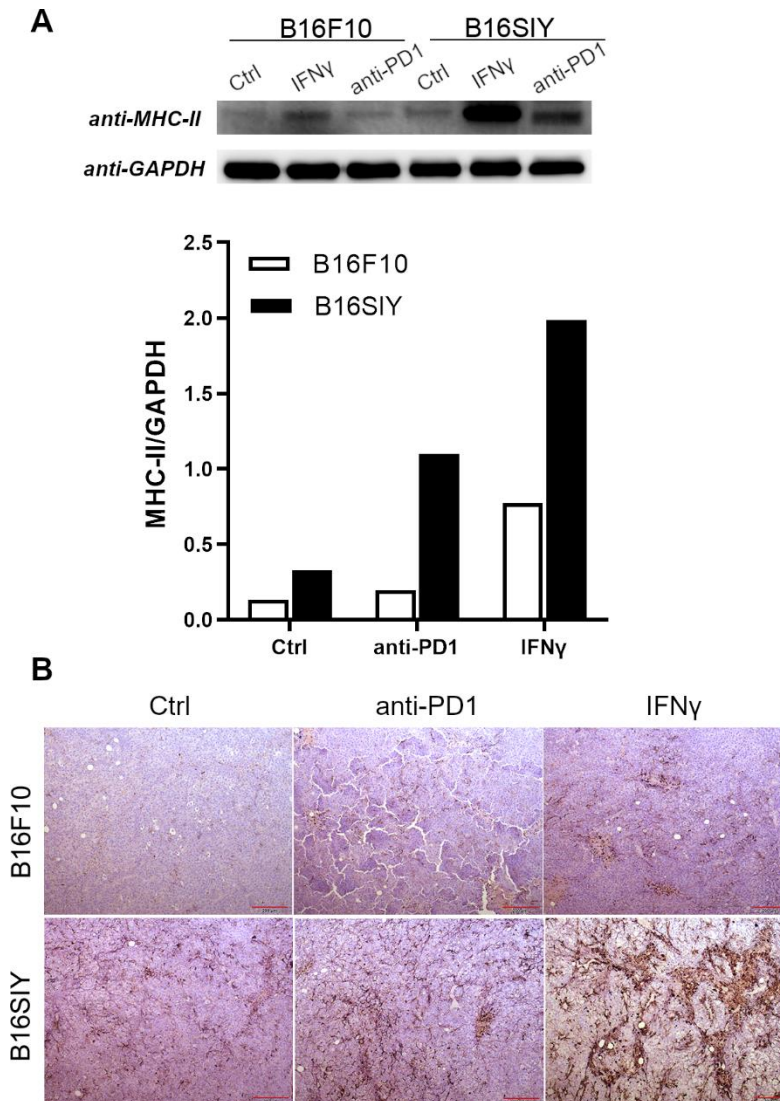


FIGURE 4. (A) western blot of tsMHC-II expression and (B) dot density quantified by ImageJ in control, anti-PD1 treated, and IFN γ treated B16F10 and B16SIY tumors. The expression level was normalized by GAPDH across various groups; (C) immunohistochemistry staining of MHC-II in the tumors.

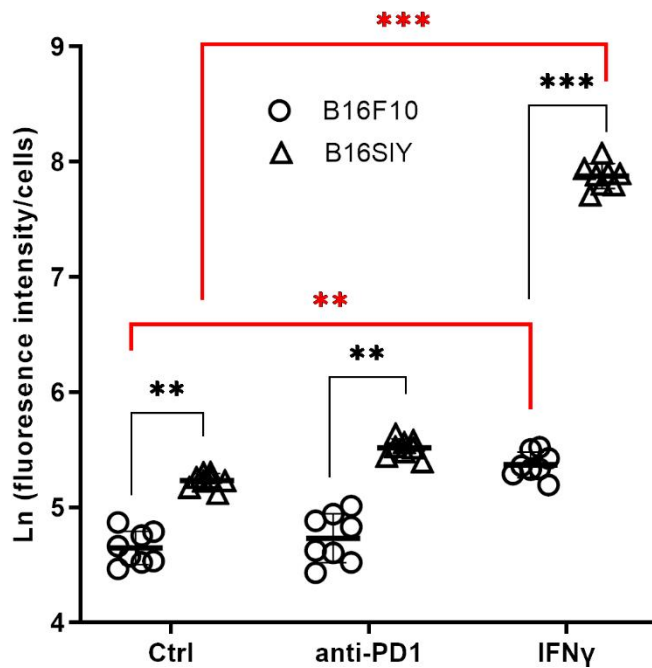
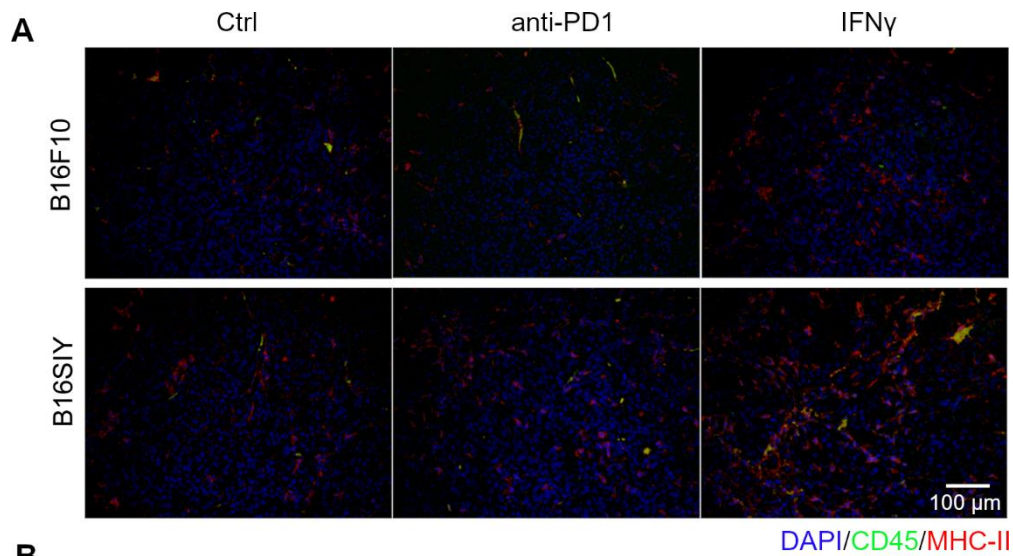


FIGURE 5. (A) immunofluorescent staining of CD45 and MHC-II in control, anti-PD1 treated, and IFN γ treated B16F10 and B16SIY tumors and (B) fluorescence intensity quantified by ImageJ; the fluorescence intensity was normalized by nucleus numbers that represent cell numbers, and the ratio was plotted as natural logarithm to compare the differences across groups. Eight different views were analyzed per sample to obtain statistics. An unpaired student t test was performed to compare: B16F10.Ctrl vs. B16SIY.Ctrl (**, $P=0.0046$); B16F10.PD1 vs. B16SIY.PD1 (**, $P=0.0031$); B16F10.IFN γ vs. B16SIY.IFN γ (***, $P<0.0001$). Meanwhile, the dynamic change

was also compared: B16F10.Ctrl vs. B16F10.IFN γ (^{##}, $P=0.0024$); B16SIY.Ctrl vs. B16SIY. IFN γ (^{###}, $P<0.0001$).

Supplemental Materials

Dynamic Tumor-Specific MHC-II Immuno-PET Predicts Checkpoint Inhibitor Immunotherapy Efficacy in Melanoma

Zhen Yang^{1,2#}, Feng Li^{1,2#}, Yuqian Huang^{2,3}, Na Yin⁴, Junjun Chu⁵, Ying Ma⁶, Roderic I. Pettigrew⁷, Dale J. Hamilton^{2,8}, Diego R. Martin^{1,9}, and Zheng Li^{1,2,9*}

#joint first authors

¹Department of Radiology, ²Center for Bioenergetics, Houston Methodist Academic Institute, Texas, USA; ³Xiangya Hospital, Central South University, Hunan, China; ⁴Department of Pediatrics, Baylor College of Medicine, Texas, USA; ⁵Department of Medicine, Keck School of Medicine, USC, California, USA; ⁶NIBIB, NIH, Maryland, USA; ⁷Engineering Medicine, Texas A&M University, Texas, USA; ⁸Department of Medicine, ⁹Department of Radiology, Weil Cornell Medicine, New York, USA

* Corresponding author:

Zheng Li, 6670 Bertner Ave, Houston, TX 77030; 713-441-7962; zli@houstonmethodist.org

First author:

Zhen Yang, 6670 Bertner Ave, Houston, TX 77030; 713-363-8494; zyang@houstonmethodist.org

Feng Li, 6670 Bertner Ave, Houston, TX 77030; 713-441-3501; fli2@houstonmethodist.org

MATERIALS AND METHODS

General

Chemical reagents and solvents were from Millipore Sigma (St. Louis, MO) and used without further purification unless otherwise stated. DOTA was from Macrocyclics (Dallas, TX). Water was purified using Milli-Q ultra-pure water system from Millipore (Milford, MA). All solvents were HPLC grade from Sigma-Aldrich (St. Louis MO, USA).

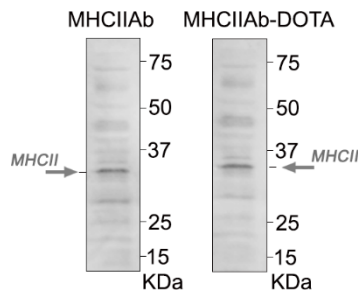
Bioreagents Source

MHC-II antibody was purchased from BioXCell (#BE0108). Rat IgG2b isotype antibody was purchased from BioXCell(#BE0090). PD1 antibody was purchased from BioXCell (#BE0273). IFN γ was purchased from Thermo Fisher Scientific (#PMC4033). Texas Red anti-rat IgG was purchased from Thermo Fisher Scientific (#T-6392). BCA Protein Assay was obtained from Thermo Fisher Scientific (#23227).

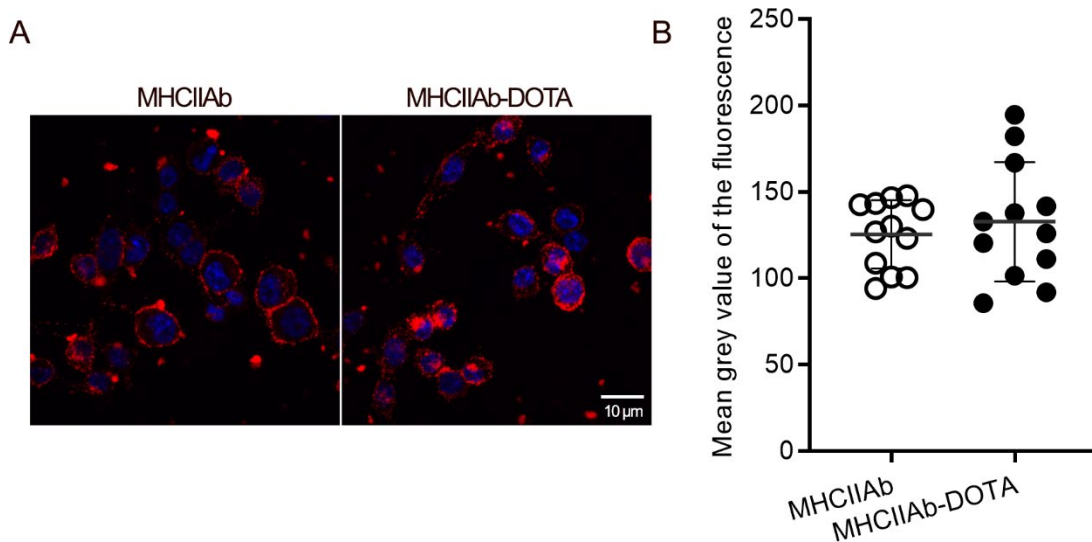
Blocking Studies for PET Imaging

Two control PET imaging studies were performed to validate the specificity of the radiotracer with the following blocking agents: (a) non-radiolabeled MHC-II antibody and (b) non-radiolabeled rat IgG2b isotype control. Specifically, cohort of B16SIY tumor-bearing mice were used in the blocking studies. Imaging, MHC-II blocking and IgG blocking were performed on three separate cohorts (n =5 per cohort). The study was performed when tumors reached $\sim 600 \text{ mm}^3$. For imaging group, approximate 3.7 MBq ^{64}Cu -DOTA-MHCII was intravenously injected into each tumor-bearing mouse, and in-line PET and CT scans were acquired at 48 h post injection (p.i.). For MHC-II blocking group, 200 μg non-radiolabeled MHC-II antibody was intravenously injected into each tumor-bearing mouse. After 30 minutes p.i. of blocking agent, approximate 3.7 MBq ^{64}Cu -DOTA-MHCII was intravenously injected into each tumor-bearing mouse, and in-line PET and CT scans were acquired at 48 h p.i. Similarly, 200 μg non-radiolabeled IgG isotype antibody was intravenously injected into each tumor-bearing mouse 30 minutes prior to the injection of the radiotracer. The radiotracer dosage was similarly as approximate 3.7 MBq, and PET/CT images were acquired at 48 p.i. PET/CT image fusion was performed with the Inveon Research Workplace. For each PET scan, regions of interest (ROIs) were drawn over the tumor on decay-corrected whole-body coronal images to derive tumor accumulation of the MHC-II immuno-PET imaging

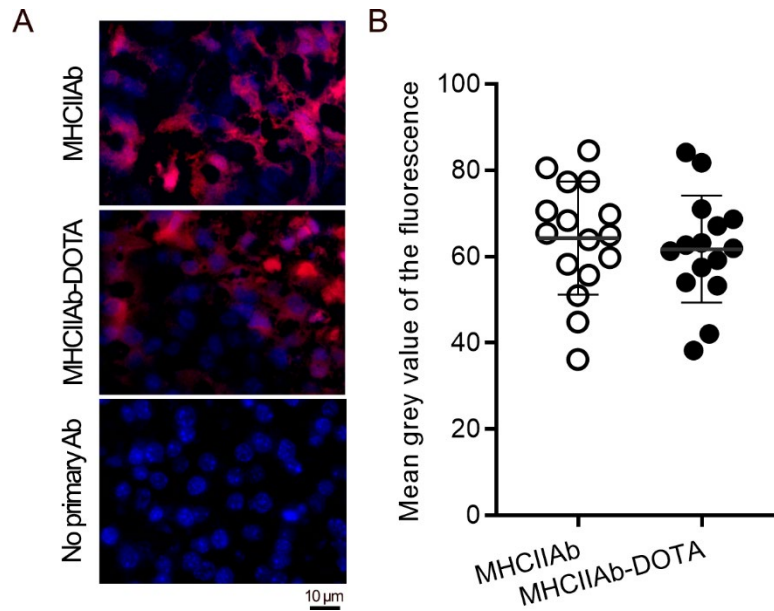
agent. The radioactivity concentration (accumulation) within tumor or organs was obtained from mean pixel values within the ROI volume and was converted to counts per milliliter per minute. Assuming a tissue density of 1 g/ml, the counts per milliliter per minute was converted to counts per gram per minute and then divided by the injected dose (ID) to obtain an imaging ROI-derived percentage of the injected radioactive dose per gram of tissue (%ID/g).



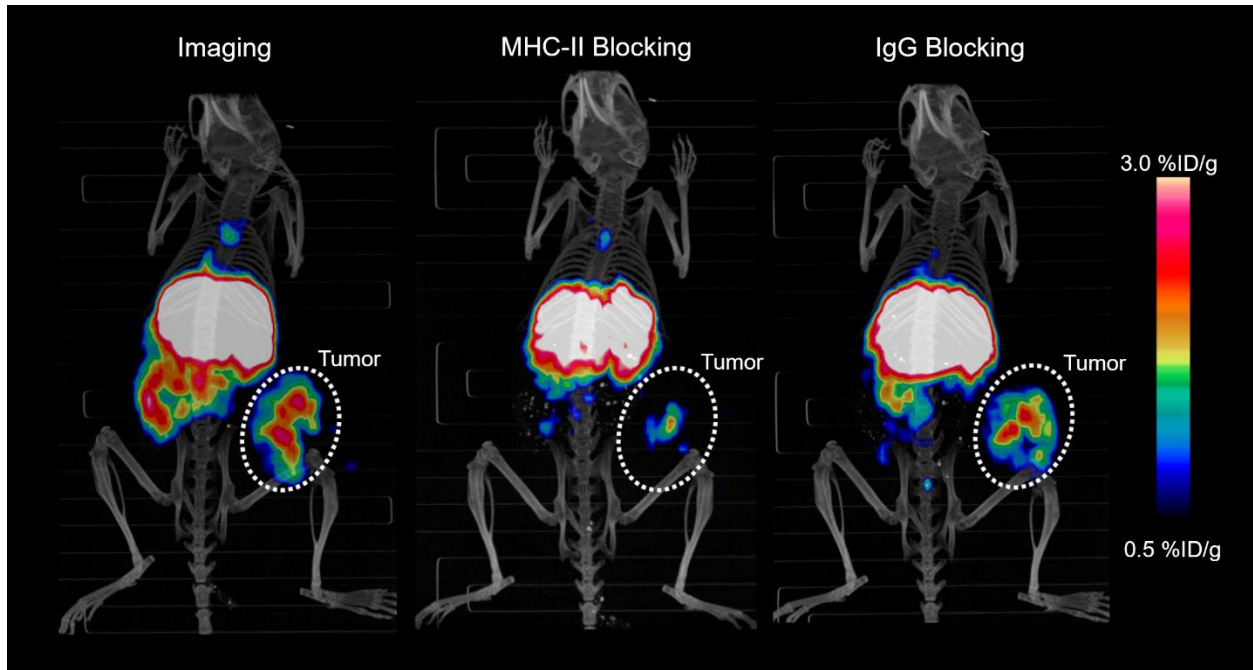
Supplemental Figure 1. Western blot of MHC-II antibody and the DOTA conjugate on protein extracts from MHC-II positive tumor tissue. No difference was observed on the immunoreactivity of the antibody and the DOTA conjugate.



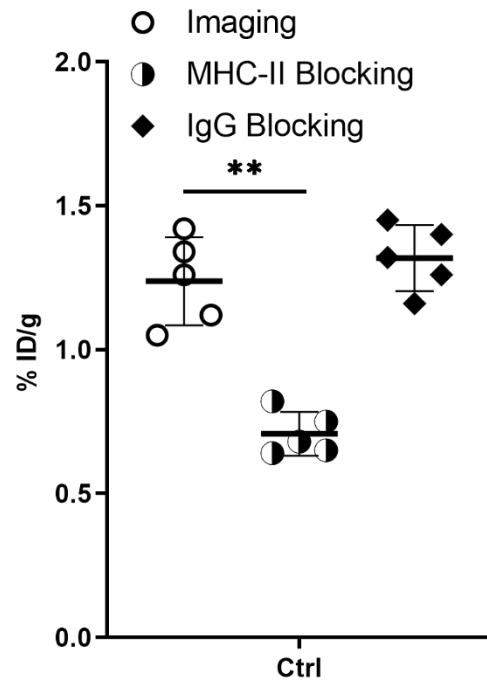
Supplemental Figure 2. Immunofluorescence staining of MHC-II antibody and the DOTA conjugate on a DC2.4 mouse dendritic cell line which typically presents antigen with high MHC-II positivity. The staining was imaged with confocal fluorescence microscopy (A). The mean fluorescence intensity in (A) was quantified and statistically analyzed to compare the significant difference (B). No significant difference was observed among the antibody and its DOTA conjugate.



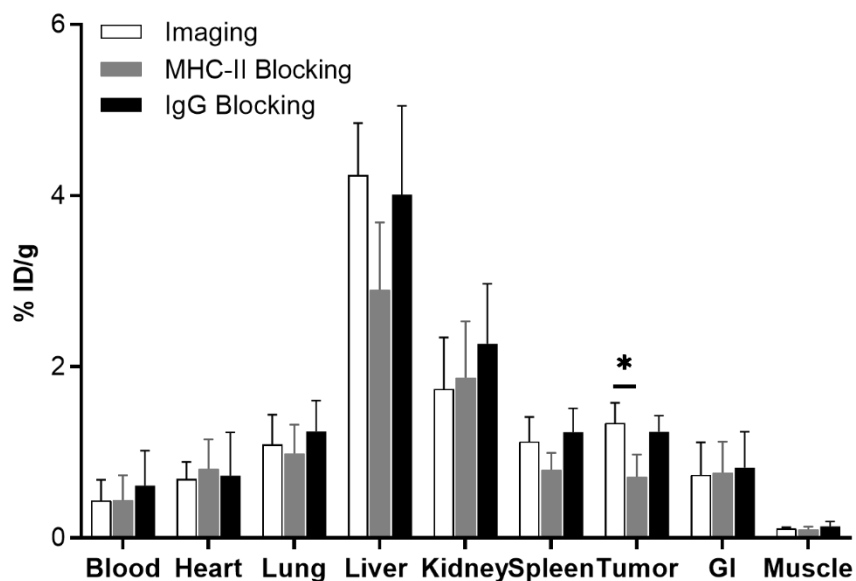
Supplemental Figure 3. MHC-II antibody immunofluorescence staining and the DOTA conjugate on B16SIY tumor tissue slides, with known MHC-II positivity. The staining was imaged with fluorescence microscopy (A). The mean fluorescence intensity in (A) was quantified and statistically analyzed to compare the significant difference (B). No significant difference was observed between the antibody and its DOTA conjugate.



Supplemental Figure 4. Noninvasive PET-CT images of B16SIY tumor-bearing mice in the blocking studies. Two types of blocking were performed: (a) excessive non-radiolabeled MHC-II antibody (MHC-II Blocking); (b) excessive rat IgG2b isotype control (IgG Blocking). The blocking agent was injected 30 minutes prior to the injection of ^{64}Cu -DOTA-MHCII radiotracer. The PET-CT image scan was performed after 48 hours injection of the radiotracer. The blocking imaging was compared to the imaging group with only radiotracer administered (Imaging).



Supplemental Figure 5. ROI quantification of tumor accumulated ^{64}Cu -DOTA-MHCII in PET images ($n = 5$ per group). Three groups were analyzed and compared: imaging group with only radiotracer administrated (Imaging); blocking study with excessive non-radiolabeled MHC-II antibody administrated prior to injection of the radiotracer (MHC-II Blocking); blocking study with excessive rat IgG2b isotype control administrated prior to injection the radiotracer (IgG Blocking). An unpaired student t test was performed to compare: MHC-II Blocking vs. Imaging (**, $P = 0.00126$).



Supplemental Figure 6. Biodistribution of ^{64}Cu -DOTA-MHCII in the PET blocking studies. Three groups were analyzed and compared: imaging group with only radiotracer administered (Imaging); blocking study with excessive non-radiolabeled MHC-II antibody administered prior to injection of the radiotracer (MHC-II Blocking); blocking study with excessive rat IgG2b isotype control administered prior to injection the radiotracer (IgG Blocking). An unpaired student t test was performed to compare: MHC-II Blocking vs. Imaging (*, $P = 0.0283$). Gastrointestinal is abbreviated as GI.